Neo-crystallization of clay minerals in the Alhama de Murcia Fault (SE Spain): implications for fault mechanics

ISABEL ABAD[1,*], JUAN JIMÉNEZ-MILLÁN[1], CATALINA SÁNCHEZ-ROA[1], FERNANDO NIETO[2] AND NICOLÁS VELILLA[3]

[1] *Departamento de Geología and CEACTierra, Unidad Asociada IACT (CSIC-UGR), Universidad de Jaén, Campus Las Lagunillas s/n, 23071 Jaén, Spain*

[2] *Departamento de Mineralogía y Petrología and IACT (CSIC-UGR), Facultad de Ciencias, Universidad de Granada, Avda. Fuentenueva s/n, 18002 Granada, Spain*

[3] *Departamento de Mineralogía y Petrología, Facultad de Ciencias, Universidad de Granada, Avda. Fuentenueva s/n, 18002 Granada, Spain*

Running head: Neo-crystallization of clays in Alhama de Murcia Fault

*E-mail: miabad@ujaen.es

ABSTRACT: Two preferred textures were observed in the Alhama de Murcia fault rocks: (a) foliated bands (>100 μm thick) rich in well crystallized dioctahedral micas, quartz, hematite and dolomite and (b) ultrafine-grained bands (<100 μm thick) made of

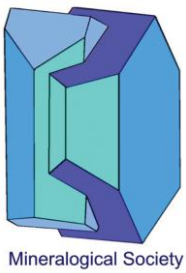

This is a 'preproof' accepted article for Clay Minerals. This version may be subject to change during the production process.
DOI: 10.1180/clm.2019.2.

patches composed of small mica crystals (< 15μm) and dispersed Fe-oxides. In both textures, kaolinite forms intergrowths or patches of randomly oriented crystals filling gaps or opening layers of presumably inherited detrital mica crystals, which is interpreted as an epitaxial growth from fluids. The Na/K ratio of mica crystals in the thin ultrafine-grained bands shows a wider range than the micas from the foliated bands including muscovitic, intermediate Na-K and paragonitic compositions. The absence of the 0.98 nm intermediate peak in the diffractograms indicates that the small micas are submicroscopically paragonite and phengite intergrowths. The d_{001} of the K-dioctahedral micas in the <2μm and whole fractions are clearly different between them. The d_{001} of micas of the <2μm fraction are greater, indicating a higher K and lower Na content in the small micas. Their composition corresponds to lower temperatures, suggesting their growth during some genetic episode in the own fault. The textural relationships indicate a late growth of kaolinite, probably by the fluid-rock interaction along fault planes and fractures. The new clay minerals could alter the stability of the fault plane. The absence of expandable clay minerals and the relatively high frictional strength of kaolinite under wet conditions could explain the observed velocity-neutral behavior of this gouge and earthquake propagation towards the surface.

Keywords: Alpujárride, electron microscopy, EPMA, friction, kaolinite, mica.

INTRODUCTION

The collision of the Eurasian and the African plates makes the southern Iberian Peninsula a tectonically active area. Many active faults are recognized, including the Alhama de Murcia, Baza, Carboneras and Palomares faults, some of which have been recently responsible for large magnitude earthquakes, e.g. the 5.1-magnitude Lorca

Earthquake in May 2011. This seism caused significant damage in the Murcia region, leaving a total of nine deaths and an estimated four hundred injured.

The internal structure of these major strike slip fault zones has been thoroughly studied (Alhama de Murcia: Masana *et al.*, 2004; Baza: Alfaro *et al.* 2008; Carboneras: Faulkner *et al.*, 2003 and Rutter *et al.*, 2012; Palomares: Booth-Rea *et al.*, 2004; among others), but less attention has been given to mineralogical and microstructural characterization and to the physical processes related to the accommodation of the deformation in the mineral phases in fault rocks (see for example for Carboneras and Palomares faults: Jiménez-Millán *et al.*, 2015 and Abad *et al.*, 2017).

The role of phyllosilicates within active fault systems and in relation to earthquake dynamics is specifically a field of ongoing research. The brittle deformation of rocks in active fault systems increases the interaction between low-temperature fluids and rocks and frequently causes an enrichment of clay minerals (illite, chlorite, smectite and interstratifications of these clays) (Evans & Chester, 1995; Solum *et al.*, 2003; Torgersen & Viola, 2014). Understanding the genetic relations affecting clays in low-temperature geological environments is complicated by the absence of chemical equilibrium, the small grain-size, which makes textural studies difficult, and the identification of common intergrowths of phases. Some of the key factors controlling active deformation processes in large fault zones are: 1) the clay mineral assemblages, 2) the chemical composition and swelling behavior of clay minerals, and 3) the influence of clay minerals on fluid circulation properties (e.g. Sibson, 1986; Vrolijk & van der Pluijm, 1999). In addition, the occurrence of clay-rich fault rocks has been suggested as contributing to the weakening of faults (Wang, 1984; Imber, 2001; Lockner *et al.*, 2011), and is possibly a controlling factor in governing seismic stick-slip versus creep mechanisms (Faulkner *et al.*, 2003; Schleicher *et al.*, 2010; Torgersen &

Viola, 2014) due to their low friction coefficients, continuous layers of water on their main cleavage planes and their velocity dependence behavior (mechanical stability under friction) (Lockner *et al.*, 2011; Schleicher *et al.*, 2013).

In this study, X-ray diffraction, scanning and transmission electron microscopy and electron microprobe have been used to characterize the fault rock mineralogy of the most seismic segment of the Alhama de Murcia Fault, placing special emphasis on the clay mineralogy. This petrographic characterization of fault rocks aims to determine the potential neoformation of clay minerals during faulting and to evaluate the possible influence of the mineralogy, specially the phyllosilicates, on the seismic activity and frictional properties of this fault (see Niemeijer & Vissers, 2014).

GEOLOGICAL SETTING AND MATERIALS

The Betic Cordillera (southern Spain) is the westernmost European Alpine chain. This ENE–WSW–trending fold-and-thrust belt is composed of the External Zone and the Internal Zone, or Alboran domain (Fig. 1a). The External Zone is characterized by Mesozoic to Tertiary rocks corresponding to the Iberian Plate palaeomargin, situated on top of the Variscan basement. The Internal Zone consists of a thrust stack of metamorphic complexes affected by major tectonism and large displacements during the early Miocene (Sanz de Galdeano, 1990). Superimposed on these structures are Neogene to Quaternary sediments fill the intramontane basins, limited by E–W and NE–SW faults (Montenat & Ott D'Estevou, 1995). Moreover, Middle Miocene to Pleistocene calc-alkaline to K-rich volcanic rocks crop out in the Cabo de Gata area (Duggen *et al.*, 2004).

The Neogene and Quaternary faulting activity in the southeastern Iberian Margin (Trans-Alboran Shear Zone) is dominated by a large NE–SW left-lateral strike-slip fault

system, which is responsible for the intense deformation of the alpine crystalline protoliths. The biggest sinistral strike-slip faults are the Carboneras Fault (Bell *et al.*, 1997), the Palomares Fault (Booth-Rea *et al.*, 2004) and the Alhama de Murcia Fault (Martínez-Díaz *et al.*, 2012) (Fig. 1). This system is, by far, the longest continuous fault system mapped in the Betic Cordillera and, therefore, would be expected to generate large-magnitude earthquakes (Gracia *et al.*, 2006). However, seismicity in the area is mainly characterized by low- to moderate-magnitude events. Nevertheless, occasional large destructive earthquakes have occurred in the region and, therefore, comprise significant earthquake and tsunami hazards to the coasts of Spain and North Africa (IGN, 2001; Masana *et al.*, 2004).

The Alhama de Murcia Fault (AMF) trends NE-SW with a 55°-65° NW dip and extends for 100 km from the Huercal-Overa depression to the outskirts of Murcia (Fig. 1). The history of the AMF reflects the tectonic inversion from an extensional to a strike-slip tectonic setting that occurred in the eastern Betics (Ferrater *et al.*, 2015). The change of regime promoted that Pliocene to Quaternary large strike-slip faults reactive previous Late Miocene normal faults associated with NW–SE and NE–SW extension (Meijninger & Vissers, 2006) within a diffuse plate boundary where African and Eurasian plates currently converge at a rate between 4 and 5 mm/yr (Alfaro *et al.*, 2012). From the Late Miocene to the present, the faulted basement has been folded and uplifted (Alfaro *et al.*, 2012), and strike-slip tectonics dominate especially, along the NE–SW faults. According to Meijninger & Vissers (2006) the AMF initiated its activity during Late Miocene, thus producing an "intra-Tortonian unconformity"; the presence of tilted sediments underlying this unconformity cut by extensional normal faults suggests that the AMF should have specifically started its activity after Tortonian. The oldest alluvial fans related to the AMF deposited during the Pleistocene indicating that

strike-slip activity and folding associated with the AMF probably initiated in the Pliocene or Quaternary (Meijninger & Vissers, 2006).

According to Martínez-Díaz *et al.* (2012), the AMF is subdivided into four segments: (1) Goñar-Lorca (37 km), with moderate concentration of epicenters and the evident relief of the Las Estancias range, (2) Lorca-Totana (16 km), where the fault controlled the evolution of the Neogene Lorca basin and Quaternary sediments are trapped by the recent activity of the fault, and with the maximum concentration of seismicity, (3) Totana-Alhama de Murcia (17 km), and (4) Alhama de Murcia-Alcantarilla (23 km) which controlled the evolution of a depression to the NW, but shows little geomorphologic fault expression.

A total of 27 samples were collected from the Lorca-Totana segment (Fig. 1b, Table 1). The Lorca-Totana segment is a 16 km long structure composed of two main NE-SW fault branches: (1) a northwestern steeply dipping reverse fault (70° NW) bounding the La Tercia range to the SE, and (2) a southeastern left-lateral and high-angle reverse fault dipping to the SE with oblique slip. The studied samples belong to the first fault branch, where the fault deforms the Alpujárride Complex, one of the thrust stacks of the metamorphic complexes within the Betic Internal Zone. The samples were taken directly from the fault plane of the AMF, including a trench recently uncovered after the 2011 earthquake (Fig. 2). During the collection, the outer 10–20 cm of material was removed to avoid any contamination of samples by surface weathering.

METHODOLOGY

X-ray diffraction (XRD) data were obtained from random powders and oriented aggregates (whole-rock samples and <2μm fraction) after washing with distilled water to remove salts. Oriented aggregates were prepared by sedimentation on glass slides and

the <2μm fraction was separated by centrifugation. Ethylene glycol treatment was carried out to permit the identification of expandable minerals (smectite, interstratified layers, etc.).

X-ray diffractograms were obtained in a PANalytical X'Pert Pro diffractometer (CuKα radiation, 45 kV, 40 mA) equipped with an X'Celerator solid-state linear detector, using a step increment of 0.008° 2θ and a counting time of 10 s/step (Department of Mineralogy and Petrology, University of Granada). A sweep between 3° and 62° 2θ was made on the dry samples, while for the glycolated samples the sweep was done between 2° and 30° 2θ in order to confirm the identification of expandable minerals. Basal spacing of micas (d_{001}) was precisely determined on the (00,10) reflection, using the own quartz of the sample as internal standard.

Following the XRD, carbon-coated polished thin sections were examined by Scanning Electron Microscopy (SEM), using back-scattered electron (BSE) imaging in atomic number contrast mode and energy-dispersive X-ray (EDX) analysis to obtain textural and chemical data. These observations were carried out with a Merlin Carl Zeiss SEM at the Centro de Instrumentación Científico-Técnica, CICT (University of Jaén) and a Leo 1430-VPSEM, at the Centro de Instrumentación Científica, CIC (University of Granada). An accelerating voltage of 20 kV, with a beam current of 1-2 nA and counting time of 50 s were used to analyse the silicates by SEM, using the following standards: albite (Na), periclase (Mg), wollastonite (Si and Ca), and orthoclase (K), and synthetic Al_2O_3 (Al), Fe_2O_3 (Fe) and $MnTiO_3$ (Ti and Mn). Analytical data were ZAF corrected. Electron microprobe (EPMA) analyses of micas corresponding to different textural zones were obtained using wavelength-dispersive spectroscopy (WDX) on a Cameca SX100 at the CIC (University of Granada). The instrument was set at an accelerating voltage of 15 kV, with a beam current of 15 nA and an electron beam

diameter of <5 μm. Data were reduced using the procedure of Pouchou & Pichoir (1985) and the standards used were albite, sanidine, periclase, diopside, quartz, vanadinite, rutile, fluorite and synthetic oxides (Al_2O_3, Fe_2O_3, NiO and $MnTiO_3$).

3 mm copper rings with a 1 mm hole in diameter were glued with an epoxy resin to the areas selected for further study by high resolution transmission electron microscopy (HRTEM). After drying for 24 hours, the rings were removed by heating the thin section. The rings were cleaned and ion-thinned to a suitable thickness for TEM study in a Fischione-1010 ion mill (CICT, University of Jaén). The initial conditions for the ion thinning were 12°, 5 Kv and 5 mA until the first hole opened, from there they had an intermediate stage with 8°, 4 Kv and 5 mA, followed by a final stage with 5°, 3 Kv and 5 mA.

The HRTEM data was obtained using the Philips CM20 (STEM) microscope, operated at 200 kV and with a point-to-point resolution of 0.27 nm in TEM mode and 5 nm in STEM mode at the CIC (University of Granada).

RESULTS

XRD analyses of the powders and oriented aggregates (bulk-rock samples and clay fraction) show that all samples contain high amounts of K- and Na-dioctahedral micas and small amounts of quartz. Carbonates (calcite and/or dolomite), gypsum, chlorite and hematite are present only in some samples (Fig. 3). There were no significant changes after ethylene glycol solvation, indicating the absence of expandable clays such as smectite except for minimal amounts in two samples. Kaolinite is present in all samples (Table 1).

Polished thin sections from the fault rocks show that they are composed of very fine-grained and well-developed gouge material (Fig. 4).

Specifically, rocks from the fault core are made of:

a) Foliated bands, >100 µm thick, that are rich in well crystallized muscovite, paragonite and quartz including dolomite and hematite crystals frequently >20 µm size (Fig. 5a). In some cases, dolomite grains exhibit intact cores, but rims with localized disaggregation, holes and Fe-oxide crystallization (Fig. 5b).
b) Thin ultrafine-grained bands (<100 µm thick) that are characterized by the presence of numerous holes and vesicles (Fig. 5c). These domains are made of patches of small crystals (<15 µm) with mica bulk composition. These patches host dispersed crystals of Fe-oxide and a network of dolomite skeletal crystals (Fig. 5d and e).
c) Patches of kaolinite made of randomly oriented crystals ranging in size from 30 µm to <2 µm and usually filling gaps in the rock structure (Fig. 5b). Kaolinite can also be observed in foliated bands associated with K- and Na-micas, following their same orientation and sometimes intergrown in stacks (Fig. 5e and f).

At TEM scale, the mineralogical characterization of the samples confirms the data obtained by XRD and SEM. Some areas contain large and well-crystallized packets of dioctahedral micas (several hundreds of nm) with 2M polytype (Fig. 6a), probably related to the thick foliated bands described by SEM. There are also smaller mica grains (<100 nm) with strain contrast orthogonal or oblique to the lattice fringes likely generated by tectonic stress (Fig. 6b and c). Kaolinite packets forming aggregates of parallel and sub-parallel grains were identified inside voids (Fig. 7a). In addition, the electron diffractions show that in some areas paragonite, muscovite and kaolinite form parallel or low-angle intergrowths at the nanoscale (Fig. 7b), although this is not so obvious in the lattice fringe images due to the fast beam damage of the kaolinite

packets. Fe-oxide aggregates, formed by randomly oriented and prismatic grains, were also identified at nanometer scale (Fig. 8).

Chemical analyses obtained by SEM-EDX and EPMA give very similar results (Table 2, Fig. 9). Dioctahedral micas include both K- and Na-dioctahedral micas. K-dioctahedral micas corresponding to the foliated bands with well crystallized crystals are characterized by compositions typical of muscovites or phengites rather than illites. The phengitic component is the main responsible for the negative correlation between Al and Fe+Mg (Fig. 9a). The sum of interlayer cations is in most cases higher than 0.85 a.p.f.u (Fig. 9b) and some of the analysed K-micas have significant Na contents (up to 0.30 a.p.f.u.) (Fig. 9c-d). The mica crystals analysed in the thin ultrafine-grained bands have also a sum of interlayer cations very similar to the well crystallized grains of the foliated bands (Fig. 9b). Nevertheless, the Na/K ratio shows a rather wider range than the micas from the foliated bands (Fig. 9c-d), covering all the field of intermediate compositions between K and Na. They show in general a larger variation in chemical composition, whereas the well crystallized crystals from the foliated bands show much less differences. Muscovitic, phengitic, intermediate Na-K and paragonitic compositions have been identified in the ultrafine-grained bands with predominance of the intermediate Na-K micas (Table 2, Fig. 9). In addition, in Figure 9, chemical data corresponding to the 2M K- dioctahedral micas from the Alpujárride protolith in the area of Sierra Espuña (Abad *et al.*, 2003) have been included for comparison.

The trioctahedral chlorites, which have a Fe/(Fe+Mg) ratio around 0.60, correspond mainly to chamosite (Fe-rich) variety (Table 3). Octahedral sums are near 6, which preclude the application of chlorite geothermometry, as such values render the margin of error of the method unacceptable; however, they, together with the low Si contents,

are characteristic of high temperature chlorites (Vidal *et al.*, 2016; Bourdelle & Cathelineau, 2015).

Kaolinite analyses fit to the theoretical formula with a pure Al-rich composition (Table 3).

DISCUSSION

Neoformation of clay minerals in the Alhama de Murcia Fault

The compositional differences between the well-crystallized packets of dioctahedral micas (mostly muscovites with some phengitic component) and the mica crystals analysed in the thin ultrafine-grained bands, with predominance of intermediate compositions between muscovite and paragonite (Figs. 9 and 10), suggest a different origin for the two of them. The compositions determined by electron microprobe for the micas of the thin ultrafine-grained bands are well inside the compositional gap between muscovite and paragonite (Guidotti *et al.*, 1994; Coggon & Holland, 2002; Parra *et al.*, 2002). They could correspond to the so-called interstratified paragonite/muscovite (Frey, 1969, 1978) or metastable intermediate sodium potassium mica (Jiang & Peacor, 1993), later interpreted by Livi *et al.* (2008) as white mica nanodomains. Nevertheless, such mineral entity is characterized in all the described cases (cited references) by an intermediate peak at 0.98 nm, which in the Alhama Fault samples is completely absent. The area of the diagrams corresponding to the (00,10) peaks of micas shows two well differentiated peaks, corresponding respectively to muscovite (or phengite) and paragonite (Fig. 3, inset). Therefore, the small mica crystals shown in the thin ultrafine-grained bands (Fig. 10a) can be interpreted only as submicroscopically paragonite and phengite intergrowths, under the resolution of compositional maps (Figs. 10b, c and d) and analysis of electron microprobe (Fig. 9), frequently described in the literature (e.g. Shau *et al.*, 1991; Livi *et al.*, 2008 and references therein). In conclusion, the most of

the compositions of the thin ultrafine-grained bands determined by electron microprobe and SEM do not correspond to individual mica grains, but represent mixed-compositions of a fine intergrowth between Na and K micas, under the resolution of EMPA and SEM analyses (~ 2μm).

To be able to compare the real Na-K content of the micas in the thin ultrafine-grained bands with that of the foliated bands, we have used an indirect approach, free of effects of their mutual contamination. As K has a significantly bigger atomic radius than Na, the d_{001} of micas is deeply influenced by the Na/K ratio (Guidotti et *al.*, 1992). The lattice parameters depend on the average compositions of the minerals at the lattice level, hence they are free of effects of the mutual contamination by the two micas. The measurement of the d_{001} parameter of the K- dioctahedral micas in oriented aggregates of the <2μm and whole fractions allows to consider if the former include predominantly the small micas of the thin ultrafine-grained bands, while the latter include the two kinds of micas (foliated and ultrafine-grained bands). The data we have obtained show a clear difference between the two populations (Fig. 11), with the d_{001} of micas of the <2μm fraction being greater, which indicates a higher K and lower Na content (Guidotti *et al*., 1992) of the small micas of the thin ultrafine-grained bands. As the two extreme terms of the muscovite-paragonite solvus are present (Fig. 3), more extreme compositions, that is higher K in muscovite limb of the solvus, represent lower temperature (Guidotti *et al.*, 1994; Coggon & Holland, 2002; Parra *et al.*, 2002). This lower temperature should be responsible of the very small grain size of the components of the intergrowth between K and Na micas. We can conclude that the micas of the thin ultrafine-grained bands have a different composition of those of the foliated bands and this composition corresponds to a lower temperature origin. Therefore, the micas in the thin ultrafine-grained bands are not the simple result of the breaking and reorientation of

the bigger metamorphic-origin micas of the original rocks, but they have grown during some genetic episode in the own fault. The fairly wide range of values of phengitic content of micas inherited from the protolith at sample level is a common characteristic of the Alpujárride rocks and is a consequence of the isothermal decompression path followed by the Alpujárride Complex from at least 10 kbar (Azañón & Crespo-Blanc, 2000).

Chlorite is the other common phyllosilicate in the Alpujárride rocks. In the fault samples, all the analyzed chlorites show low Si content and octahedral sums near 6 (Table 3), which are indices of respectively high amesite and low sudoite components, which, in turn, indicate a high temperature of formation of the chlorites, but preclude an exact determination of the temperature (Vidal *et al.*, 2016; Bourdelle & Cathelineau, 2015). Therefore, similarly to the micas of the foliated bands, chlorites in the fault rocks show the chemical characteristics of those of the protolith (Abad et al. 2003), suggesting a metamorphic origin.

In fact, the protolith of the studied rocks is a grey phyllite, widely distributed in all the Alpujarride Complex, which can be described from the nearest outcrops in the southern part of Sierra Espuña (Fig. 1b). These rocks are composed by K- and Na- dioctahedral micas, chlorite, quartz, hematite, carbonates (calcite and dolomite) and retrograde smectite (Nieto *et al.*, 1994). The high amounts of K- and Na- micas in the fault rocks is consistent with the mineralogy of the protolith, characterized in detail by Abad *et al.* (2003). Nevertheless, the textural differences between the Alpujárride protolith and the fault rocks are remarkable: a well-developed foliation in the phyllites affecting even quartz, oxide and carbonate grains (see for example Fig. 3 in Abad *et al.* 2003) against the very fine-grained breccias in the fault rocks (Figs. 4 and 5). In addition, to our knowledge, kaolinite has not been described in any protolithic sample, which contrasts

with its ubiquitous presence in all the samples collected in or near the fault plane (Table 1).

The presence of authigenic kaolinite must be related to the fluid-rock interaction along fault planes and fractures. In some cases, kaolinite is finely intergrown with small mica crystals (Figs. 5e, 5f and 7b). In Figure 5e it can be appreciated how the newly formed kaolinite opens the layers of presumably inherited detrital mica crystals. This has been traditionally interpreted as an epitaxial growth from fluids, in which the mica layers act as a template facilitating kaolinite growth (see Arostegui *et al.*, 2001 and references therein). In other cases, kaolinite forms patches of randomly oriented crystals filling gaps in the rock structure. We have not found any proof of transformation of previous mica by kaolinite by means of a topotaxial mechanism. Overall, the textural relationships between mica and kaolinite indicate that the latter grew after the former, from a fluid. Given the stability field of kaolinite, its growth was a low-temperature process (< 200 ºC); if such a process is related to the final step of the hydrothermal activity in the fault or it is the result of meteoric infiltration, is difficult to establish with the available data.

The role of clay minerals in the mechanical behavior of the fault

Niemeijer & Vissers (2014) studied the frictional properties of the AMF rocks that ruptured during the 2011 earthquake, which included fault gouges and elongated lenses of phyllites from the protolith embedded in a cataclastic matrix. They identified higher frictional strength in the protolith-derived lenses (μ from 0.5 to 0.7 at room temperature and from 0.7 to 0.8 at elevated temperatures) than the gouge-derived samples (μ from 0.35 to 0.6 at room temperature and from 0.4 to 0.5 at elevated temperatures). The lower friction coefficients are consistent with the larger amounts of weak phyllosilicates

identified in the gouges, which in addition to contributing to fault weakness also impact the mechanical stability of the fault under shear. The mechanical stability is also known as the velocity- or rate-dependence, where the friction rate parameter (a-b) describes the stability of the sliding surface. A positive value of (a-b) indicates velocity-strengthening leading to fault creep, while negative values of (a-b) correspond to velocity-weakening that may result in earthquake nucleation (Scholz, 1998). According to Niemeijer & Vissers (2014), gouges from the AMF show velocity strengthening properties which migrate to a velocity-neutral value under simulated shallower conditions. However, the protolith-derived lenses show velocity-weakening properties, which suggest that earthquakes in the AFM are nucleated in these protolith-derived lenses. The occurrence of phyllosilicates or other weak minerals in a fault zone can promote distributed deformation and provide an explanation for fault weakness (Faulkner *et al.*, 2003, 2010; Colletini *et al.*, 2009).

Fragile behavior of stronger minerals with high friction values and velocity-weakening behaviour such as quartz ($0.6 < \mu < 0.7$, Byerlee, 1978; Dieterich & Kilgore, 1994) can lead to cataclastic textures that increase rock permeability and create permeable paths. Fluid-rock interaction within the paths produce leaching of the host rocks and favor the crystallization of new minerals: submicroscopically paragonite and phengite intergrowths located in the thin ultrafine-grained bands and the rounded to lens-shaped micropods of kaolinite. In addition to the mineral changes, the interaction of low temperature fluids and the fault rocks modifies microstructural features of the gouges and could, as a consequence, alter the stability of the fault plane.

In particular, the authigenesis of expandable clay minerals in fault gouges can contribute to friction coefficients as low as 0.05 under wet conditions, as well as to velocity-strengthening behaviors (Lockner *et al.*, 2011). For this reason, the expandable

minerals have often been related to fault creep and mechanical stability, as in the case of the central segment of the San Andreas Fault (Lockner *et al.,* 2011). Nevertheless, the AFM shows no evidence of authigenesis of expandable minerals in its fault gouges. On the contrary, all authigenic minerals are non-expandable. The frictional strength of kaolinite under wet conditions is high when compared with the expandable clay minerals: μ=0.51 (Moore & Lockner, 2004), μ=0.53 (Morrow *et al.,* 2000), μ=0.29 (Behnsen & Faulkner, 2012), and μ= 0.23 (Brantut *et al.,* 2008).

As suggested by frictional data (Niemeijer & Vissers, 2014), earthquake nucleation in the AMF is concentrated in lenses of phyllitic basement rocks; immediately after, rupture propagation takes place through the fault rocks. The absence of smectite within the fault gouges (only small amounts of smectite were identified in two of the studied samples) and the presence of kaolinite, quartz and micas can explain the observed velocity-neutral behavior of this gouge and earthquake propagation towards the surface (Niemeijer & Vissers, 2014) instead of the velocity-strengthening behavior characteristic of weak phyllosilicates that is expected to represent a barrier to rupture propagation.

ACKNOWLEDGMENTS

We would like to thank J.A. López Martín for his time and advice during the sampling and Dr. M.M. Abad-Ortega and A. Martinez-Morales for their support in electron microscopy data acquisition. The critical reviews and very helpful comments and suggestions of S.H. Haines and E. Torgersen have notably improved the quality of the paper. This work has been financed by Investigation Projects CGL2011-30153-C02-01 and CGL2011-30153-C02-02 from MINECO, Research project UJA2014/06/17 from the Universidad-Caja Rural de Jaén, Research Groups RNM-179 and RNM-325 of the

Junta de Andalucía, and the FPI scholarship BES-2012-052 562 from the Spanish Government (MINECO).

REFERENCES

Abad I., Nieto F., Peacor D.R. & Velilla N. (2003) Prograde and retrograde diagenetic and metamorphic evolution in metapelitic rocks of Sierra Espuña (Spain). *Clay Minerals*, **38**, 1–23.

Alfaro P., Delgado J., Sanz de Galdeano C., Galindo-Zaldívar J., García-Tortosa F.J., López-Garrido A.C., López-Casado C., Marín C., Gil A. & Borque M.J. (2008) The Baza Fault: a major active extensional fault in the Central Betic Cordillera (South Spain). *International Journal of Earth Sciences*, **97**, 1353–1365.

Alfaro P., Delgado J., García-Tortosa F.J., Lenti L., López A., López-Casado C. & Martino S. (2012) Widespread landslides induced by the Mw 5.1 earthquake of 11 May 2011 in Lorca, SE Spain. *Engineering Geology*, **137-138**, 40–52.

Arostegui J., Irabien M.J., Nieto F., Sangüesa J. & Zuluaga M.C. (2001) Microtextures and the origin of muscovite-kaolinite intergrowths in sandstones of the Utrillas Formation, Basque Cantabrian Basin, Spain. *Clays and Clay Minerals*, **49**, 529–539.

Azañón J.M. & Crespo-Blanc A. (2000) Exhumation during a continental collision inferred from the tectonometamorphic evolution of the Alpujárride Complex in the central Betics (Alborán Domain, SE Spain). *Tectonics*, **19**, 549–565.

Behnsen J. & Faulkner D. (2012) The effect of mineralogy and effective normal stress on frictional strength of sheet silicates. *Journal of Structural Geology*, **42**, 49–61.

Bell J.W., Amelung F. & King G.C.P. (1997) Preliminary Late Quaternary slip history o the Carboneras fault, southeastern Spain. *Journal of Geodynamics*, **24**, 51–66.

Booth-Rea G., Azañón J.M., Azor A. & García-Dueñas V. (2004) Influence of strike-slip fault segmentation on drainage evolution and topography. A case study: the

Palomares fault zone (southeastern Betics, Spain). *Journal of Structural Geology*, **26**, 1615–1632.

Bourdelle F. & Cathelineau M. (2015) Low-temperature chlorite geothermometry: a graphical representation based on a *T*-R^{2+} diagram. *European Journal of Mineralogy*, **27**, 617–626.

Brantut N., Schubnel A., Rouzaud J.N., Brunet F. & Shimamoto T. (2008) High-velocity frictional properties of a clay-bearing fault gouge and implications for earthquake mechanics. *Journal of Geophysical Research*, **113**, B10401.

Byerlee J. (1978) Friction of rocks. *Pure and Applied Geophysics*, **116**, 615–626.

Coggon R. & Holland J.B. (2002) Mixing properties of phengitic micas and revised garnet-phengite thermobarometers. *Journal of Metamorphic Geology*, **20**, 683–696.

Collettini C., Niemejer A., Viti C. & Marone C. (2009) Fault zone fabric and fault weakness. *Nature*, **462**, 907–910.

Collettini C., Viti C., Tesei T. & Mollo S. (2013) Thermal decomposition along natural carbonate faults during earthquakes. *Geology*, **41**, 927–930.

Dieterich J.H. & Kilgore B.D. (1994) Direct observation of frictional contacts: new insights for state-dependent properties. *Pure and Applied Geophysics*, **143**, 283–302.

Duggen S., Hoernle K. & van der Bogaard H. (2004) Magmatic evolution of the Alboran region: The role of subduction in forming the western Mediterranean and causing the Messinian Salinity Crisis. *Earth and Planetary Science Letters*, **218**, 91–108.

Evans J.P. & Chester F.M. (1995) Fluid-rock interaction in faults of the San Andreas system; inferences from San Gabriel Fault rock geochemistry and microstructures. *Journal of Geophysical Research*, **100**, 13007–13020.

Faulkner D.R., Jackson C.A.L., Lunn R.J., Schlische R.W., Shipton Z.K., Wibberley C.A.J. & Withjack M.O. (2010) A review of recent developments concerning the structure, mechanics and fluid flow properties of fault zones. *Journal of Structural Geology*, **32**, 1557–1575.

Faulkner D.R., Lewis A.C. & Rutter E.H. (2003) On the internal structure and mechanics of large strike-slip fault zones: field observations from the Carboneras fault, southeastern Spain. *Tectonophysics*, **367**, 235–251.

Ferrater M., Booth-Rea G., Pérez-Peña J.V., Azañón J.M., Giaconia F., Masana E. (2015) From extension to transpression: Quaternary reorganization of an extensional-related drainage network by the Alhama de Murcia strike-slip fault (eastern Betics). *Tectonophysics*, **663**, 33–47.

Frey M. (1969) A mixed-layer paragonite/phengite of low-grade metamorphic origin. *Contributions to Mineralogy and Petrology*, **24**, 63–65.

Frey M. (1978) Progressive low-grade metamorphism of a black shale formation, Central Swiss Alps, with special reference to pyrophyllite and margarite bearing assemblages. *Journal of Petrology*, **19**, 95–135.

Gracia E., Pallas R., Soto J.I., *et al.* (2006): Active faulting offshore SE Spain (Alboran Sea): implications for earthquake hazard assessment in the Southern Iberian Margin. *Earth and Planetary Science Letters*, **241**, 734–749.

Guidotti C.V., Mazzoli C., Sassi F.P. & Blencoe J.G. (1992) Compositional controls on the cell dimensions of $2M_1$ muscovite and paragonite. *European Journal of Mineralogy*, **4**, 283–297.

Guidotti C.V., Sassi F.P., Blencoe J.G., & Selverstone J. (1994) The paragonite-muscovite solvus: I. P-T-X limits derived from the Na-K compositions of natural,

quasi-binary paragonite-muscovite pairs. *Geochimica et Cosmochimica Acta*, **58**, 2269–2275.

IGN (2001) Instituto Geográfico Nacional, Catálogo Sísmico Nacional hasta el 1900. Madrid, Spain.

Imber J., Holdsworth R.E., Butler C.A. & Strachan R.A. (2001) A reappraisal of the Sibson- Scholz fault zone model: the nature of the frictional to viscous ("brittle-ductile") transition along a long-lived, crustal-scale fault, Outer Hebrides, Scotland. *Tectonics*, **20**, 601–624.

Jiang W.T. & Peacor D.R. (1993) Formation and modification of metastable intermediate sodium potasium mica, paragonite, and muscovite in hydrothermally altered metabasites from North Wales. *American Mineralogist*, **78**, 782–793.

Jiménez-Millán J., Abad I., Hernández-Puentes P. & Jiménez-Espinosa R. (2015) Influence of phyllosilicates and fluid-rock interaction on the deformation style and mechanical behaviour of quartz-rich rocks in the Carboneras and Palomares fault areas (SE Spain). *Clay Minerals*, **50**, 619–638.

Livi K.J.T., Christidis G.E., Árkai P. & Veblen D.R. (2008) White mica domain formation: A model for paragonite, margarite, and muscovite formation during prograde metamorphism. *American Mineralogist*, **93**, 520–527.

Lockner D.A., Morrow C., Moore D. & Hickman S. (2011) Low strength of deep San Andreas fault gouge from SAFOD core. *Nature*, **472**, 82–85.

López Comino J.A., Mancilla F., Morales J. & Stich D. (2012) Rupture directivity of the 2011, Mw 5.2 Lorca earthquake (Spain). *Geophysical Research Letters*, **39**, L03301.

Masana E., Martínez-Díaz J.J., Hernández-Enrile J.L. & Santanach P. (2004) The Alhama de Murcia fault (SE Spain), a seismogenic fault in a diffuse plate boundary:

seismotectonic implications for the Ibero-Magrebian region. *Journal of Geophysical Research*, **109**, B01301.

Martínez-Díaz J.J., Béjar-Pizarro M., Álvarez-Gómez J.A., Mancilla F.L., Stich D., Herrera G. & Morales J. (2012) Tectonic and seismic implications of an intersegment rupture. The damaging May 11th 2011 Mw 5.2 Lorca, Spain, earthquake. *Tectonophysics*, **546-547**, 28–37.

Martínez-Díaz J.J., Masana E. & Ortuño M. (2012) Active tectonics of the Alhama de Murcia fault, Betic Cordillera, Spain. *Journal of Iberian Geology*, **38**, 269–286.

Meijninger B.M.L. & Vissers R.L.M. (2006) Miocene extensional basin development in the Betic Cordillera, SE Spain revealed through analysis of the Alhama de Murcia and Crevillente Faults. *Basin Research*, **18**, 547–571.

Montenat C. & Ott D'Estevou P. (1995) Late Neogene basins evolving in the Eastern Betic transcurrent fault zone: An illustrated review. Pp. 372–386 in: *Tertiary Basins of Spain* (P.F. Friend & C.J. Dabrio, editors). Cambridge University Press, Cambridge, UK.

Moore D. & Lockner D. (2004) Crystallographic controls on the frictional behavior of dry and water-saturated sheet structure minerals. *Journal of Geophysical Research* **109**, B03401.

Morrow C., Moore D. & Lockner D. (2000) The effect of mineral bond strength and adsorbed water on fault gouge frictional strength. *Geophysical Research Letters*, **27**, 815–818.

Niemeijer A.R. & Vissers R.L.M. (2014) Earthquake rupture propagation inferred from the spatial distribution of fault rock frictional properties. *Earth and Planetary Science Letters*, **396**, 154–164.

Nieto F., Velilla N., Peacor D.R. & Ortega-Huertas M. (1994) Regional retrograde alteration of sub-greenschist facies chlorite to smectite. *Contributions to Mineralogy and Petrology*, **115**, 243–252.

Parra T., Vidal O. & Agard, P. (2002) A thermodynamic model for Fe–Mg dioctahedral K white micas using data from phase-equilibrium experiments and natural pelitic assemblages. *Contributions to Mineralogy and Petrology*, **143**, 706–732.

Pouchou J.L. & Pichoir F. (1985) "PAP" (f) (r) (t) procedure for improved quantitative microanalysis. In: Armstrong, J.T. (ed.): Microbeam Analysis, San Francisco Press, San Francisco, 104 pp.

Rutter E.H., Faulkner D.R. & Burgess R. (2012) Structure and geological history of the Carboneras Fault Zone, SE Spain: part of a stretching transform fault system. *Journal of Structural Geology*, **42**, 227–245.

Sanz de Galdeano C. (1990) Geologic evolution of the Betic Cordilleras in the western Mediterranean, Miocene to present. *Tectonophysics*, **172**, 107–119.

Schleicher A.M., Hofmann H. & van der Pluijm B.A. (2013) Constraining clay hydration state and its role in active fault systems. *Geochemistry, Geophysics, Geosystems*, **14**, 1039–1052.

Schleicher A.M., van der Pluijm B.A. & Warr L.N. (2010) Nanocoatings of clay and creep of the San Andreas fault at Parkfield, California. *Geology*, **38**, 667–670.

Scholz C.H. (1998) Earthquakes and friction laws. *Nature*, **391**, 37–42.

Shau J.H., Feather M.E., Essene E.J. & Peacor D.R. (1991) Genesis and solvus relations of submicroscopically intergrown paragonite and phengite in a blueschist from northern California. *Contributions to Mineralogy and Petrology*, **106**, 367–378.

Sibson R.H. (1986) Earthquakes and rock deformation in crustal fault zones. *Annual Review of Earth and Planetary Sciences*, **14**, 149–175.

Solum J., van der Pluijm B., Peacor D. & Warr L. (2003) Influence of phyllosilicate mineral assemblages, fabrics, and fluids on the behavior of the Punchbowl fault, southern California. *Journal of Geophysical Research*, **108**, 2233.

Torgersen E. & Viola, G. (2014) Structural and temporal evolution of a reactivated brittle-ductile fault – Part I: Fault architecture, strain localization mechanisms and deformation history. *Earth and Planetary Science Letters*, **407**, 205–220.

Vidal O., Lanari P., Munoz M., Bourdelle F. & de Andrade V. (2016) Deciphering temperature, pressure and oxygen-activity conditions of chlorite formation. *Clay Minerals*, **51**, 615–633.

Vrolijk P. & van der Pluijm B.A. (1999) Clay gouge. *Journal of Structural Geology*, **21**, 1039–1048.

Wang C.Y. (1984) On the constitution of the San Andreas fault zone in Central California. *Journal of Geophysical Research*, **89**, 5858–5866.

Whitney D.L. & Evans B.W. (2010) Abbreviations for names of rock-forming minerals. *American Mineralogist*, **95**, 185–187.

Figures

Fig. 1

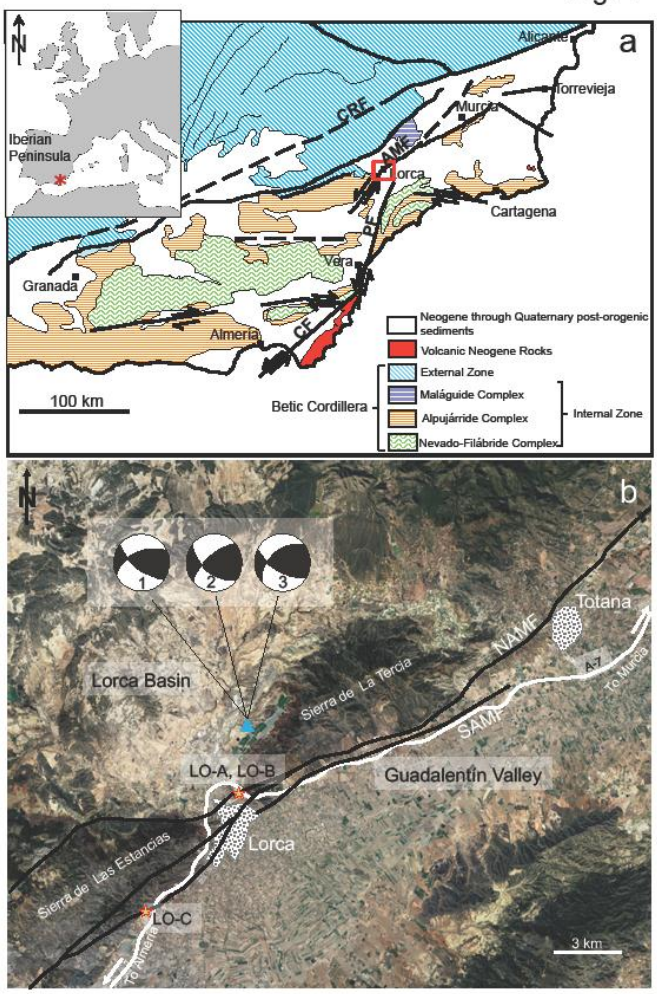

Fig. 1. (a) Geological map of the Trans-Alborán Shear Zone with the main Neogene faults (SE Spain) and the location of the study area. AMF: Alhama de Murcia Fault, CF: Carboneras Fault, CRF: Crevillente Fault and PF: Palomares Fault. Modified from Gracia *et al.* (2006). (b) Location map with the projection of the Alhama de Murcia Fault (NAMF and SAMF, Northern and Southern branches of the fault, respectively) including the sampling points (LO-A, LO-B, and LO-C). The triangle is the mainshock of the Lorca 2011 seismic sequence taken from Lopez-Comino *et al.* (2012). Focal solutions of the mainshock from several agencies are shown (1: Instituto Andaluz de Geofísica; 2: Instituto Geográfico Nacional; 3: Harvard University).

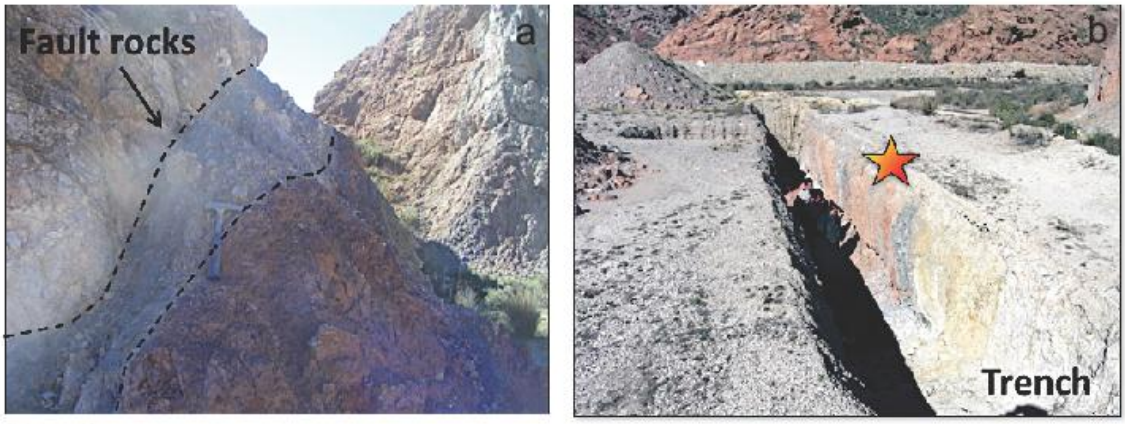

Fig. 2

Fig. 2. View of the outcrops: (a) detail of fault rocks; (b) trench where samples LOA16-19 were collected.

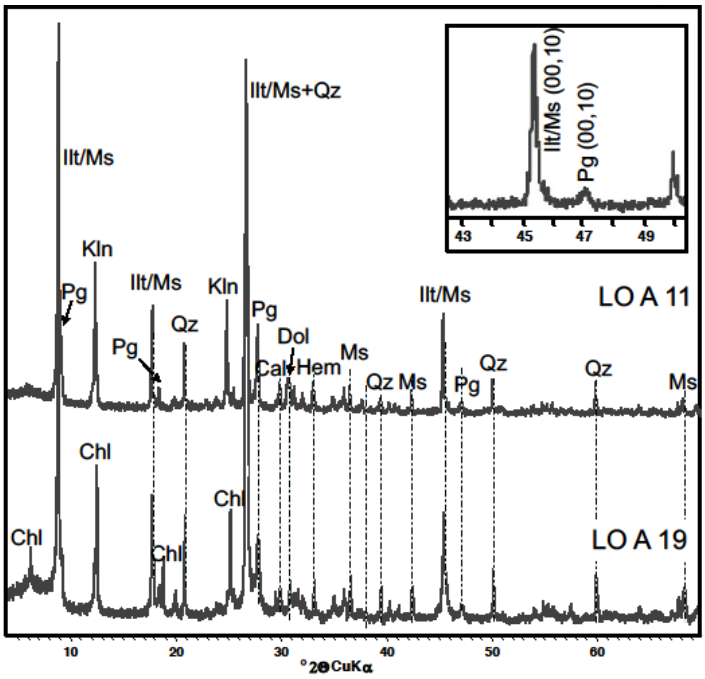

Fig. 3

Fig. 3. Representative X-ray diffractograms corresponding to samples from Alhama de Murcia fault rocks. Inset: Enlarged (00,10) mica peak region, showing the presence of only two peaks corresponding to muscovite (phengite) and paragonite.

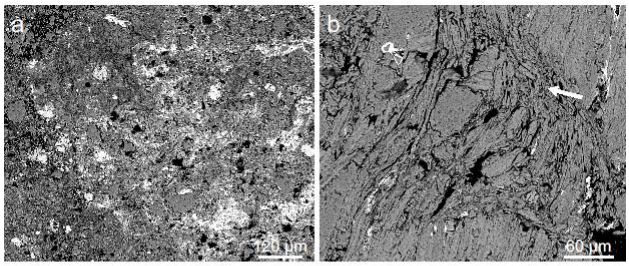

Fig. 4

Fig. 4. BSE images showing the textural aspect of the fault rocks: (a) Fine-grained material corresponding to the gouge with poorly sorted quartz grains with irregular shapes and Fe-oxides; (b) phyllosilicates stacks with curved shapes and signs of grain-size reduction (arrow).

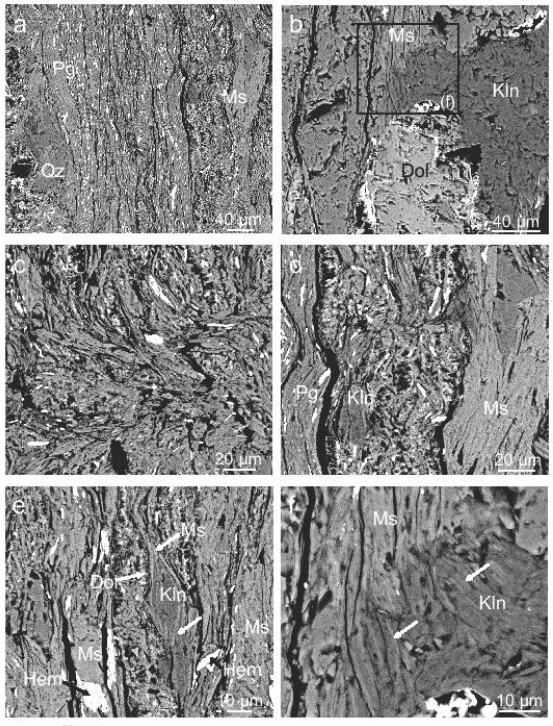

Fig. 5

Fig. 5. BSE images of the fault rocks: (a) an example of foliated band composed of micas, quartz and Fe-oxides; (b) dolomite grain showing rims with localized disaggregation and Fe-oxide crystallization, partially surrounded by a patch of kaolinite; (c) poorly crystalline material characterized by the presence of numerous holes

alternating with thin and very fine-grained phyllosilicate bands; (d) detail of the network of dolomite skeletal crystals between two foliated bands; (e) other example of the network between phyllosilicate bands, one of them with a stack of kaolinite with some K-mica packets intergrown (white arrows); (f) detail of the patch of kaolinite from the picture b, in which it is possible to distinguish mica packets intergrown with kaolinite (white arrows). Dol: dolomite; Hem: Hematite; Kln: kaolinite; Ms: K-rich dioctahedral mica; Pg: Na-rich dioctahedral mica; Qz: quartz.

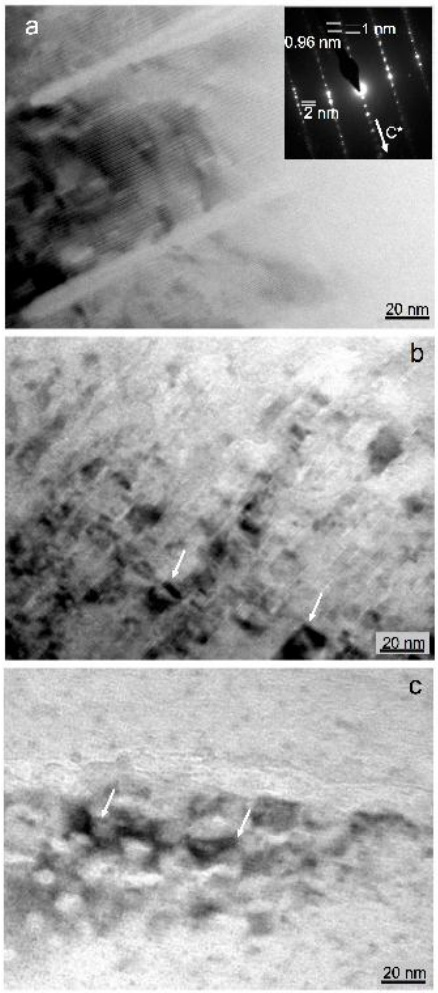

Fig. 6

Fig. 6. a) TEM lattice fringe image with large dioctahedral mica crystals showing a 2 nm periodicity; the electron diffraction pattern shows the presence of basal spacings

corresponding to paragonite (0.96 nm) and muscovite (1 nm); b) and c) TEM lattice fringes images corresponding to thin dioctahedral mica packets with a very damage appearance (see arrows).

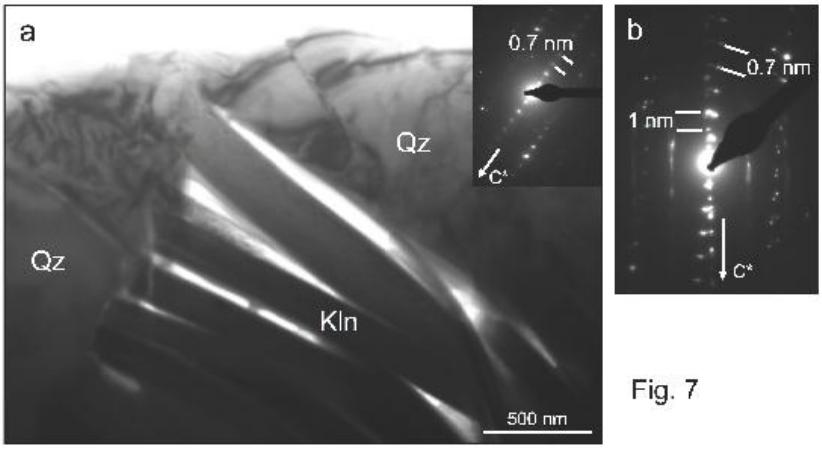

Fig. 7

Fig. 7. a) Low magnification image of kaolinite aggregate surrounded by quartz grains; b) SAED showing the parallel and sub-parallel relations between dioctahedral micas and kaolinite. Kln: kaolinite; Qz: quartz.

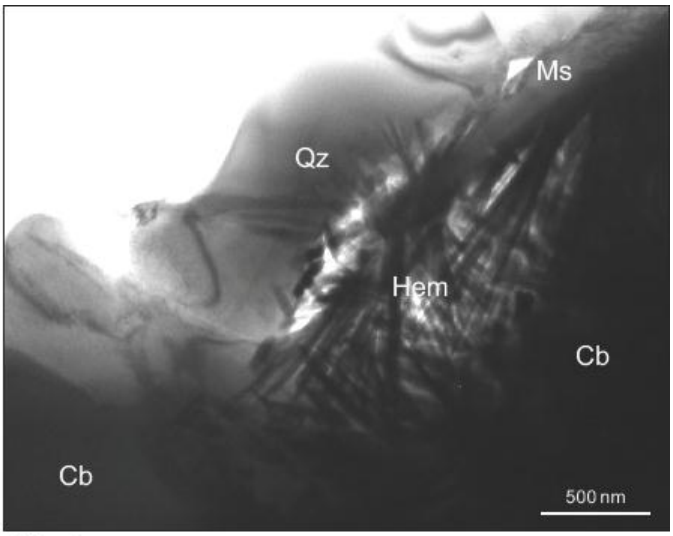

Fig. 8

Fig. 8. Low magnification image of a Fe-oxide aggregate at nanoscale. Cb: carbonates (Cal-Dol); Hem: hematite; Ms: K-rich dioctahedral mica; Qz: quartz.

Fig. 9

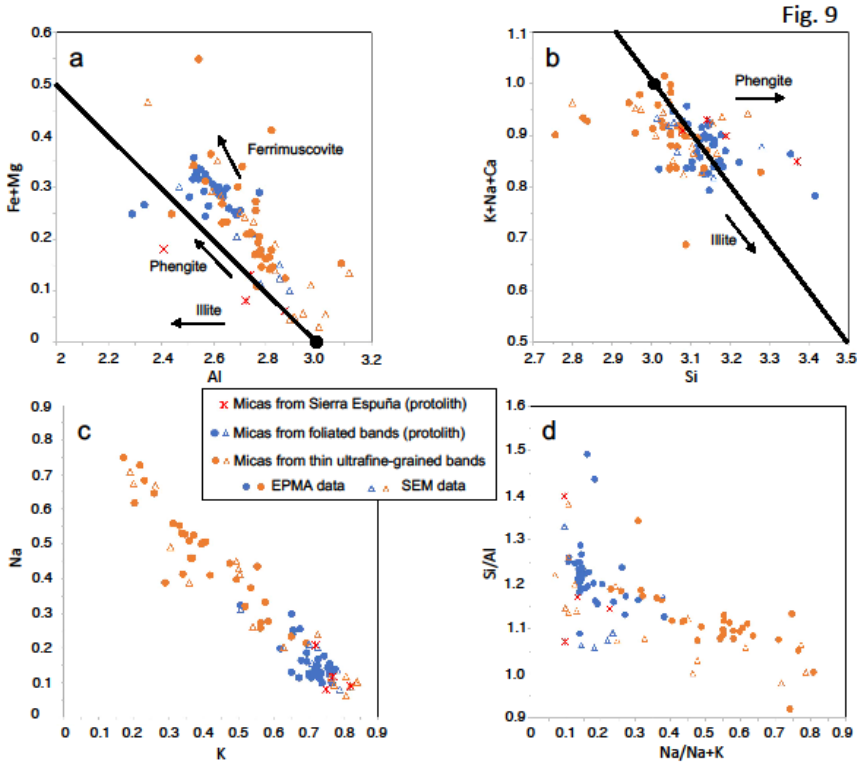

Fig. 9. Relationships among chemical components of dioctahedral micas studied by SEM/EDX and EPMA/WDX. Black circles and solid lines respectively indicate the theoretical muscovite position and corresponding exchange vectors.

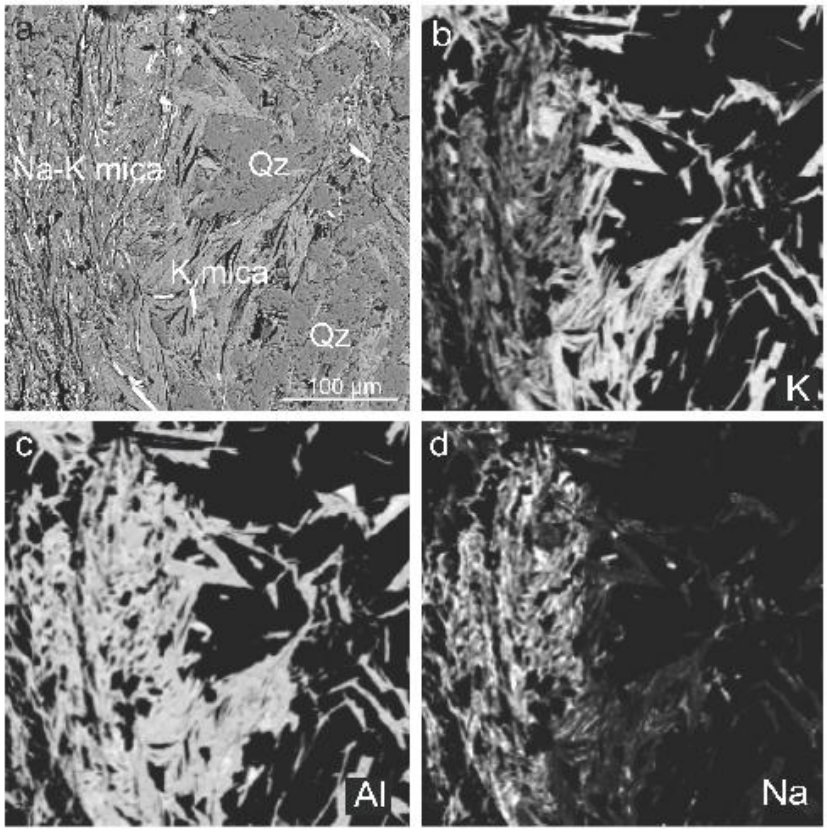

Fig. 10

Fig. 10. BSE image (a) and K, Al, and Na X-ray maps (b, c, and d, respectively) of one of the selected zones analyzed by EPMA and processed with ImageJ, where well crystallized muscovites (right) and a fine-grained phyllosilicate band mainly composed of Na-K micas (left) are observed.

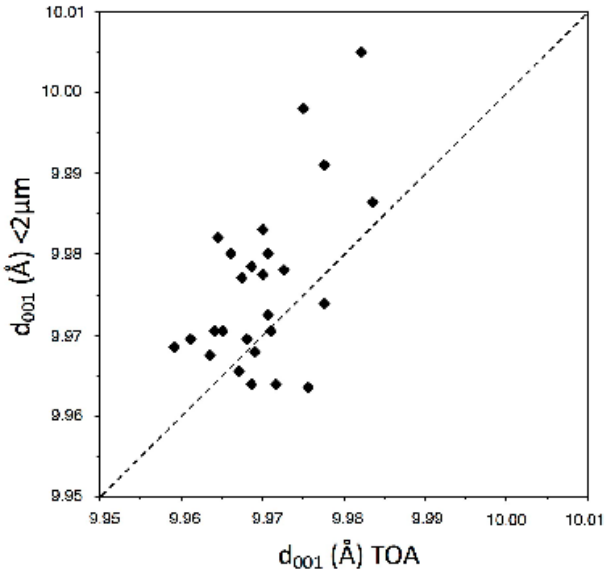

Fig. 11

Fig. 11. Comparison between the mica d_{001} spacings of the <2µm and whole fractions (TOA, total oriented aggregates) of the studied samples, calculated from the position of the (00,10) K- dioctahedral mica peak.

Tables

Table 1. Samples list of the studied rocks with the geographic coordinates and bulk mineralogy determined by XRD and SEM.

Samples	Geographic coordinates	Mineral composition (Qz, Ilt/Ms, Pg and Kln in all the samples)
LO-A-01	37° 41' 21.24" N/1° 41' 0.79" W	Chl, Cal
LO-A-02		Chl, Cal
LO-A-03		Chl, Sme, Cal
LO-A-04		Chl, Sme, Cal, Hem
LO-A-05		Dol
LO-A-06		
LO-A-07		
LO-A-08	37° 41' 19.59" N/1° 41' 05.93" W	Kfs
LO-A-09		Chl, Cal
LO-A-10		Cal
LO-A-11		Cal, Dol, Hem
LO-A-12	37° 41' 20.22" N/1° 41' 08.97" W	Cal
LO-A-13		Dol, Hem
LO-A-14		Dol, Hem
LO-A-15		Hem, Kfs
LO-A-16		Chl, Dol, Gp
LO-A-17		Chl, Dol, Gp
LO-A-18		Chl, Dol, Gp
LO-A-19		Chl, Cal, Dol, Hem
LO-B-01	37° 41' 20.31" N/1° 41' 20.89" W	Dol
LO-B-02		Chl, Hem
LO-C-01	37° 38' 16.79" N/1° 44' 47.39" W	
LO-C-02		Dol, Hem, Mws
LO-C-03		Hem
LO-C-04		Hem
LO-C-05		Hem
LO-C-06		Hem

Abbreviations of minerals name after Whitney and Evans (2010). In italic, samples studied by SEM and in bold, samples studied by HRTEM.

Table 2. Representative EPMA and SEM data for dioctahedral micas.

Electron-microprobe analyses (wt %)

	SiO_2	Al_2O_3	MgO	FeO	TiO_2	K_2O	CaO	Na_2O	Total
LO-A-14 1 G1	50.20	33.16	1.08	3.27	0.15	8.79	0.05	0.99	97.85
LO-A-14 1 G3	47.59	32.10	1.23	3.54	0.17	8.68	0.02	0.74	94.22
LO-A-14 1 G8	52.93	30.14	0.86	3.01	0.22	7.92	0.02	1.03	96.30
LO-A-14 1 G10	47.89	32.13	1.27	3.36	0.12	8.66	0.08	0.99	94.67
LO-A-14 1 G12	48.65	33.45	1.18	3.67	0.24	8.50	0.12	1.00	97.01
LO-A-14 1 G14	48.45	33.24	0.83	2.92	0.26	7.85	0.10	1.85	95.67
LO-A-14 2 G11	46.61	33.21	1.03	3.48	0.17	8.41	0.03	1.04	94.11
LO-A-14 2 G15	47.22	35.63	0.76	2.41	0.14	6.09	0.09	2.52	94.96
LO-A-14 1 P2	52.67	33.31	0.89	3.15	0.56	7.12	0.10	2.11	100.04
LO-A-14 1 P15	46.02	35.63	0.51	2.13	0.95	4.38	0.13	3.55	93.40
LO-A-14 2 P5	46.03	36.36	0.41	1.86	0.31	3.10	0.14	5.04	93.30
LO-A-14 2 P9	45.81	36.25	0.47	2.35	0.15	5.65	0.11	3.45	94.34
LO-A-14 2 P12	45.84	34.81	0.52	2.78	0.82	5.85	0.13	3.06	93.94

Structural formulae normalized to $O_{10}(OH)_2$ on the basis of SEM/EDX and EPMA/WDX data.

	Si	Al^{IV}	Al^{VI}	Fe	Mg	Ti	∑ oct.	K	Ca	Na	∑ inter.
Micas from foliated bands											
EPMA											
LO-A-14 1 G1	3.22	0.78	1.74	0.18	0.10	0.01	2.02	0.72	0.00	0.12	0.85
LO-A-14 1 G3	3.18	0.82	1.72	0.20	0.12	0.01	2.05	0.74	0.00	0.10	0.84
LO-A-14 1 G8	3.42	0.58	1.71	0.16	0.08	0.01	1.97	0.65	0.00	0.13	0.78
LO-A-14 1 G10	3.19	0.81	1.71	0.19	0.13	0.01	2.03	0.74	0.01	0.13	0.87
LO-A-14 1 G12	3.16	0.84	1.72	0.20	0.11	0.01	2.05	0.70	0.01	0.13	0.84
LO-A-14 1 G14	3.18	0.82	1.75	0.16	0.08	0.01	2.01	0.66	0.01	0.24	0.90
LO-A-14 2 G11	3.12	0.88	1.75	0.20	0.10	0.01	2.05	0.72	0.00	0.13	0.86
LO-A-14 2 G15	3.09	0.91	1.84	0.13	0.07	0.01	2.06	0.51	0.01	0.32	0.84
SEM											
LO-A-4 3 2	3.28	0.72	1.75	0.10	0.20	0.00	2.05	0.79	0.00	0.08	0.88
LO-A-5 1 4	3.06	0.94	1.91	0.09	0.06	0.00	2.06	0.73	0.00	0.20	0.93
LO-A-5 3 6	3.02	0.98	1.79	0.07	0.04	0.11	2.01	0.70	0.02	0.21	0.93
LO-A-5 3 7	3.04	0.96	1.89	0.08	0.04	0.03	2.04	0.78	0.00	0.14	0.92
LO-A-4 4 2	3.16	0.84	1.85	0.07	0.13	0.02	2.07	0.51	0.00	0.31	0.82
LO-C-3 1 5	3.07	0.93	1.96	0.04	0.06	0.00	2.05	0.71	0.00	0.16	0.87
Micas fron thin ultrafine-grained bands											
EPMA											
LO-A-14 1 P2	3.28	0.72	1.72	0.16	0.08	0.03	2.00	0.57	0.01	0.25	0.83
LO-A-14 1 P15	3.05	0.95	1.83	0.12	0.05	0.05	2.05	0.37	0.01	0.46	0.84
LO-A-14 2 P5	3.04	0.96	1.87	0.10	0.04	0.02	2.03	0.26	0.01	0.64	0.92
LO-A-14 2 P9	3.03	0.97	1.85	0.13	0.05	0.01	2.04	0.48	0.01	0.44	0.93
LO-A-14 2 P12	3.05	0.95	1.78	0.15	0.05	0.04	2.03	0.50	0.01	0.39	0.90
SEM											
LO-A-4 3 3	3.24	0.76	1.59	0.19	0.27	0.03	2.08	0.84	0.00	0.10	0.94
LO-A-4 5 5	3.18	0.82	1.70	0.19	0.15	0.02	2.07	0.84	0.00	0.10	0.94
LO-A-4 6 2	3.17	0.83	1.76	0.17	0.13	0.03	2.08	0.81	0.00	0.06	0.87
LO-A-4 6 3	3.16	0.84	1.78	0.17	0.11	0.00	2.07	0.81	0.00	0.12	0.93
LO-A-4 6 5	3.11	0.89	1.84	0.12	0.10	0.02	2.07	0.77	0.00	0.09	0.87
LO-C-3 1 1	3.10	0.90	1.80	0.12	0.13	0.02	2.07	0.82	0.00	0.09	0.90
LO-C-3 1 6	3.05	0.95	1.88	0.08	0.06	0.02	2.04	0.73	0.00	0.24	0.97
LO-C-3 2 6	3.10	0.90	1.82	0.09	0.15	0.02	2.08	0.76	0.00	0.12	0.88
LO-A-4 5 2	3.01	0.99	2.01	0.03	0.00	0.00	2.04	0.19	0.00	0.71	0.90
LO-A-4 5 3	2.96	1.04	1.99	0.05	0.00	0.00	2.04	0.26	0.02	0.67	0.95
LO-A-4 5 4	3.08	0.92	1.97	0.04	0.00	0.00	2.01	0.20	0.03	0.68	0.91

Table 3. Structural formulae for chlorites and kaolinites normalized to $O_{10}(OH)_8$ on the basis of SEM/EDX data.

	Si	Al^{IV}	Al^{VI}	Fe	Mg	Mn	Ti	∑ oct.
Chlorites								
LO-A-4 2 1	2.54	1.46	1.43	2.68	1.84	0.00	0.00	5.95
LO-A-4 3 4	2.72	1.28	1.51	2.65	1.69	0.04	0.00	5.89
LO-A-4 4 1	2.79	1.21	1.56	2.56	1.60	0.00	0.00	5.73
LO-A-4 6 1	2.55	1.45	1.58	2.47	1.89	0.00	0.00	5.94
Kaolinites								
LO-A-5 3 1	3.96	0.04	4.01	0.00	0.00	0.00	0.00	4.01
LO-A-5 3 5	4.04	0.00	3.94	0.00	0.00	0.00	0.00	3.94
LO-A-5 3 8	3.94	0.06	4.02	0.00	0.00	0.00	0.00	4.02